BIOCHEMISTRY

10.1126/sciadv.1600650

HU multimerization shift controls nucleoid compaction

Michal Hammel,[1]* Dhar Amlanjyoti,[2] Francis E. Reyes,[1] Jian-Hua Chen,[3] Rochelle Parpana,[1] Henry Y. H. Tang,[1] Carolyn A. Larabell,[1,3] John A. Tainer,[1,4]* Sankar Adhya[2]

Molecular mechanisms controlling functional bacterial chromosome (nucleoid) compaction and organization are surprisingly enigmatic but partly depend on conserved, histone-like proteins HUαα and HUαβ and their interactions that span the nanoscale and mesoscale from protein-DNA complexes to the bacterial chromosome and nucleoid structure. We determined the crystal structures of these chromosome-associated proteins in complex with native duplex DNA. Distinct DNA binding modes of HUαα and HUαβ elucidate fundamental features of bacterial chromosome packing that regulate gene transcription. By combining crystal structures with solution x-ray scattering results, we determined architectures of HU-DNA nucleoproteins in solution under near-physiological conditions. These macromolecular conformations and interactions result in contraction at the cellular level based on in vivo imaging of native unlabeled nucleoid by soft x-ray tomography upon HUβ and ectopic HUα38 expression. Structural characterization of charge-altered HUαα-DNA complexes reveals an HU molecular switch that is suitable for condensing nucleoid and reprogramming noninvasive *Escherichia coli* into an invasive form. Collective findings suggest that shifts between networking and cooperative and noncooperative DNA-dependent HU multimerization control DNA compaction and supercoiling independently of cellular topoisomerase activity. By integrating x-ray crystal structures, x-ray scattering, mutational tests, and x-ray imaging that span from protein-DNA complexes to the bacterial chromosome and nucleoid structure, we show that defined dynamic HU interaction networks can promote nucleoid reorganization and transcriptional regulation as efficient general microbial mechanisms to help synchronize genetic responses to cell cycle, changing environments, and pathogenesis.

INTRODUCTION

Bacterial and archaeal chromosomes exist in a microscopically visible, variably condensed nucleoid entity analogous to eukaryotic chromatin (*1*, *2*). Similar to histones in eukaryotes, nucleoid-associated proteins (NAPs) are essential for bacterial nucleoid condensation and resulting expression patterns (*3*, *4*). HU, a ubiquitous bacterial histone-like protein, is among the most conserved and abundant NAPs in eubacteria (*5*). In *Escherichia coli*, HU forms a dimer by HUα self-association (HUαα) or by HUα-HUβ (HUαβ) interactions. HUα is mostly expressed during the early exponential growth phase and HUβ is expressed only during the stationary phase (*6*), supporting the importance of distinct HUαα/DNA and HUαβ/DNA packaging of the nucleoid in regulating expression patterns during growth and stasis. HU dimers show high affinity to specialized or damaged DNA structures [for example, kinked or cruciform DNA (*7*, *8*)], but it is as a largely sequence-independent DNA binding protein that HU has key architectural roles in DNA nucleoid compaction and in constraining negative supercoils in DNA (*9*), but this has remained structurally undefined. DNA supercoiling modulates gene transcription in a promoter-specific way (*10*) and influences gene expression in many pathogens (*11*). Moreover, nucleoid organization into local topological domains contributes to its overall compactness (*2*, *9*) and to transcriptional regulation by enigmatic mechanisms that are directly connected. Global transcription profiles change when bacterial cells transition from the lag phase to the exponential growth phase (*12*–*14*), and HU regulates these changes. Yet, despite notable efforts to unravel the molecular mechanisms of HU interactions with DNA that affect the nucleoid state, structures with undamaged, nonspecific DNA remain unknown and the molecular connections between HU-DNA interactions and nucleoid architecture that regulate gene expression remain mysterious (*2*).

A noninvasive *E. coli* strain can be switched to an invasive form solely by mutational changes in HU (*15*, *16*). Mutations in HUα residues E38K and V42L (termed HUα38) transform the *E. coli* nucleoid and reorganize the transcriptional program to activate mammalian cell invasion–associated factors, such as the curly fiber encoding gene products (*15*, *16*); thus, HU interactions with DNA can affect global transcriptional regulation and key processes, such as pathogenesis.

HUαα homodimers are mostly present during the lag and exponential growth phase, whereas HUαβ heterodimers are mostly present during the early and late stationary phases. The exchange of HUαα with HUαβ influences the corresponding gene expression pattern [reviewed by Dorman (*2*)]. HU binds at high affinities (in the nanomolar range) to specific DNA structures that are of limited occurrence and that have specific gene regulatory or recombination functions. However, HU molecules (~50,000 molecules per cell) far outnumber such specific binding sites; thus, DNA structure and sequence-independent binding of HU likely predominate its functions in bacterial DNA condensation.

To help elucidate the fundamental and mechanistic components of bacterial chromosome structure (packing) and function (transcription), we first determined the crystal structures of the complexes of HUαα, HUαβ, and HUα38α38 with a nonspecific DNA duplex with random sequences (Fig. 1). To determine the functional relationships of these HU-DNA structures to DNA networks and nucleoid architecture, we characterized the overall organization of HU's nucleoprotein complexes

[1]Molecular Biophysics and Integrated Bioimaging, Lawrence Berkeley National Laboratory, Berkeley, CA 94720, USA. [2]Laboratory of Molecular Biology, Center for Cancer Research, National Cancer Institute, National Institutes of Health, Bethesda, MD 20892, USA. [3]Department of Anatomy, University of California San Francisco, San Francisco, CA 94143, USA. [4]Department of Molecular and Cellular Oncology, The University of Texas MD Anderson Cancer Center, 1515 Holcombe Boulevard, Houston, TX 77030, USA. *Corresponding author. Email: mhammel@lbl.gov (M.H.); jatainer@lbl.gov (J.A.T.)

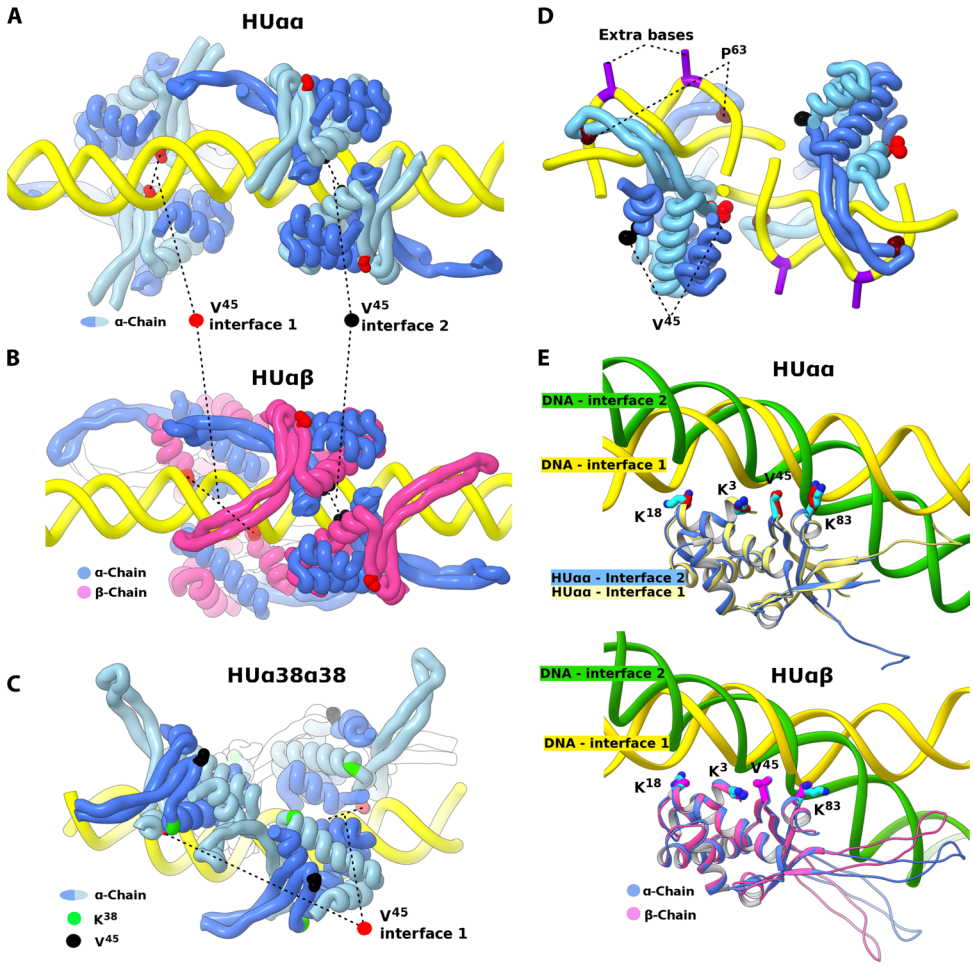

Fig. 1. HU-DNA crystal structures, functional interactions, and interfaces. (**A** to **C**) Crystal structures of HUαα-DNA, HUαβ-DNA, or HUα38α38-DNA for four asymmetric units across continuous DNA are colored as indicated. V^{45} inserts into the DNA minor groove as shown for interfaces 1 and 2. The E38K mutation site in the HUα38α38-DNA structure is highlighted (green). (**D**) Two asymmetric units of the *Anabaena* HUαα crystal structure bound to a distorted DNA substrate. The positions of DNA, extra bases, residue P^{63}, and V^{45} are colored as indicated. (**E**) Superimposition of HUαα-DNA and HUαβ-DNA interfaces. The protein portion was superimposed to highlight different DNA paths.

in solution by small-angle x-ray scattering (SAXS) (*17*). We found that HUαα, HUαβ, and HUα38α38 organize DNA differently, in ways suitable for bacteria to use dynamic transformations of HU nucleoprotein networks to control DNA supercoiling and to thereby modify transcriptional programming. To test whether these changes in DNA binding by HU can affect the nucleoid state at the cellular level, we imaged unlabeled DNA in vivo by soft x-ray tomography (SXT). Comparisons of bacterial cells with HUβ and HUα38 expression show that the specific HUα38 mutations that affect DNA binding and pathogenesis have a marked impact on nucleoid structure at the cellular level.

RESULTS AND DISCUSSION

Distinct HU-DNA interfaces reveal plasticity in nucleoid packing

Crystallization of HU with native duplex DNA has eluded researchers for over a decade. We therefore used SAXS (*17*, *18*) to optimize nonspecific DNA interactions with HU in solution and efficiently approach effective crystallizations of solution interactions with a suitable order for structure determination (see Materials and Methods). We thereby crystallized and determined structures of HUαα, HUαβ, and HUα38α38 in complex with 19– or 20–base pair (bp) DNA at resolutions of 2.7 to 3.5 Å (Fig. 1, fig. S1, and table S1). Structures of HU-DNA complexes were solved by molecular replacement with the structure of HUαα (*19*) or HUαβ (*20*) (table S1). All of these structures show linear DNA conformation across HU's α-helical "body" (Fig. 1, A to C, and fig. S1) rather than bent DNA located between extended β-ribbon "arms" as seen for structurally specific DNA interactions with two appropriately placed extrahelical bases (*21*) (Fig. 1, A to C, and movie S1). The asymmetric unit contains one dimer and one DNA strand that is paired to a symmetry-related strand with the out-of-register duplex positions, such that backbones superimpose but base identity differs. This "virtual sliding" of DNA along HU means that complexes with either 19- or 20-bp DNA show identical continuous DNA electron density in the unit cell (fig. S1). All HU dimers adopt similar secondary structures forming two HU faces. Crystallographic symmetry reveals an assembly in which each HU face bound to different DNA duplexes (Fig. 1E and fig. S2). All HU

dimers bind DNA through locking a DNA phosphate between the G^{46} and K^{83} peptide amides and inserting V^{45} into the minor groove (phosphate lock) (Fig. 1E and fig. S2). The importance of the G^{46} and G^{82}-K^{83} backbone in the locking mechanism explains their strict conservation among prokaryotes (fig. S3). In contrast, the previously described intercalation of P^{63} on the extended arms with the DNA minor groove may be a lock-and-key mechanism for specific limited DNA sites (*22*) (Fig. 1D). The interactions defined here seem universal for the sequence-independent DNA binding acting in nucleoid compaction. Unlike HU interaction with structurally specific aberrant DNA (Fig. 1D), interaction with native B-form DNA does not stabilize the extended arms, evidently distinguishing specific aberrant DNA complexes from nucleoid compaction complexes. The weak electron density of the extended arms at the contact regions is consistent with limited DNA interactions, allowing functionally important flexibility for sequence-independent DNA interactions (fig. S1).

HU interactions with native DNA trigger HU multimerization, which promotes straightening of the DNA axis, and not bending, as seen for individual HU dimers on structurally aberrant DNA (Fig. 1 and fig. S1). Two HUααs interact across the DNA in opposite orientations, primarily through a hydrogen bond network (fig. S1). Alternating HUαα-HUαα couples lie alongside the DNA (in the 20-bp distance) oriented oppositely to the first couple (Fig. 1A). These HUαα-HUαα couples interact with two distinct DNA-protein interfaces, with ~30° difference in the tilt of the HUαα-HUαα couple relatively to the main DNA axis (fig. S2A). Although V^{45} inserts into the DNA minor groove at both sites, variability in the interfaces suggests that V^{45} acts as the fulcrum of a ball-and-socket joint, permitting tilt and twist of HUαα on DNA (Fig. 1E and fig. S2B). V^{45} is replaced by arginines in HU family members that are DNA-specific binders [R^{58} of Hbb and R^{46} of IHF (integration host factor) β chain] to stabilize DNA with a specific TTA sequence (*23*, *24*) (fig. S2D). Arginines insert into the DNA minor groove and explain higher binding affinities (*7*) compared to the sequence-independent flexible valine ball-and-socket joint.

The α and β chains share 69% sequence similarity (fig. S3A), forming two HUαβ faces (αβ and βα) (Fig. 1, B and E). Two HUαβs bind across the DNA to form an HUαβ-HUαβ couple. However, the couple at the other side of the DNA is in close contact with the first couple facing the same direction (Fig. 1B). Alternating HUαβ-HUαβ couples adopt distinct protein-DNA interfaces resembling interface 1 or 2 in the HUαα homodimer (Fig. 1E and figs. S2B and S4). Interface 1 is formed by αβ and interface 2 is formed by the βα protein face. In contrast, mutant HUα38α38 adopts a substantially different arrangement along the DNA with two HUα38α38 couples lying along the same side of the DNA within close proximity (Fig. 1C). Although only one face of HUα38α38 supports formation of continuous DNA through interface 2, weak electron density for noncontinuous DNA is visible at the opposite face (fig. S1C). This marked rearrangement of HU mutant along DNA, without perturbing the DNA-protein interface, suggests the plasticity of HU multimerization along native DNA.

Parallel DNA networking dominates nucleoid packing in growth phase

By combining multiple HUαα-DNA asymmetric units perpendicular to the DNA, we visualized lateral protein multimerization (Fig. 2A). Alternating lateral multimers form a DNA network that can grow in both lateral and medial directions (Fig. 2B and movie S2). To test this networking in solution, we measured SAXS on mixtures of HUαα with 20- and 80-bp DNA duplexes at varied protein/DNA ratios. SAXS profiles show strong diffraction peaks, confirming the formation of periodic nucleoprotein networks in solution (Fig. 2B and fig. S5). Diffraction at d = 50, 57, 78, and 2 × 78 Å spacings corresponds to the distances between the DNAs. SAXS curves of HUαα–20-bp DNA complexes show sharper peaks due to a more ordered assembly, with peaks matching the first-order diffractions of the crystal structure. Diffraction peaks for low HUαα/DNA ratios (fig. S5) suggest HU's capability to network DNA, with several HUααs mimicking concentration in cells. Mutations of the HUαα-HUαα interface (K38E, V42L, and E34K) completely diminished diffraction peaks, suggesting a critical role of HUαα-HUαα coupling in DNA networking (Fig. 2C). Mutation of the HUαα-DNA interface (G82E and V45E) does not disrupt the DNA network (Fig. 2C and fig. S5). However, introducing the G82E and K83E double mutation at the phosphate lock leads to a disruption of the network (Fig. 2C), most likely due to weakened DNA affinity (Fig. 2D). The P63E mutation on the extended arms diminished diffraction peaks at d ~78 Å and d ~ 2 × 78 Å, which suggests disruption of medial multimerization, although the d ~57 Å peak indicates persistence of lateral multimerization (Fig. 2C). The extended and disordered character of the arms is suitable for allowing multiple interactions with neighboring DNAs or HUααs that were disrupted by P63E mutation. This observation uncovers an independent role for HU arms or body in forming dynamic networks. Such dynamic DNA networking mediated by HU may explain efficient nucleoid compaction in rapidly growing bacteria. Moreover, overproduction of HUαα or HUαβ does not increase nucleoid condensation (*9*). Thus, collective data support a model for nucleoid condensation specific to the early bacterial lag and exponential growth phase in which DNA is organized into a network maintained by sparsely bound HUαα. Protein-free gaps may allow the efficient exchange of various DNA metabolic proteins and other NAPs required for exponential growth phase–specific condensation of the bacterial chromosome (fig. S9) (*9*).

HUαα and HUαβ interplay allows dynamic changes in nucleoid architecture

By combining multiple HUαβ-DNA asymmetric units along the continuous DNA, we modeled an assembly that fully covers double-stranded DNA (dsDNA). Although this assembly bridges the centrally located dsDNA to two flanking DNAs, the lateral HUαβ-HUαβ multimerization for DNA networking is not maintained (Fig. 3A). The β chain substitutions of K90N, E15D, and E12A, which participate in the hydrogen bonds maintaining lateral multimerization of HUααs, disrupt multimerization in HUαβ (Fig. 3B). This destabilization of the lateral multimerization permits the intercalation of arms from oppositely oriented HUs, allowing for tight condensation of HUαβ to surround DNA (Fig. 3A and movie S3).

To test this disruption of lateral multimerization in solution, we measured SAXS on the HUαβ with 80-bp DNA at various ratios. SAXS data show formation of HUαβ-DNA filaments in solution with a length of ~250 Å (Fig. 3C and fig. S6). Missing diffraction peaks in the curves support the absence of the DNA network. Atomistic models of HUαβ/80-bp DNA filaments match the 250 Å length defined by the $P(r)$ function (Fig. 3C) and fit experimental SAXS curves well (Fig. 3C and fig. S6A). The fitting of SAXS curves and SAXS-defined volumes (*25*) shows two binding modes where HUαβ fully covers DNA at high HUαβ/DNA ratios or bridges two DNAs at low ratios (Fig. 3C and fig. S6A). The two binding modes described support and extend previous

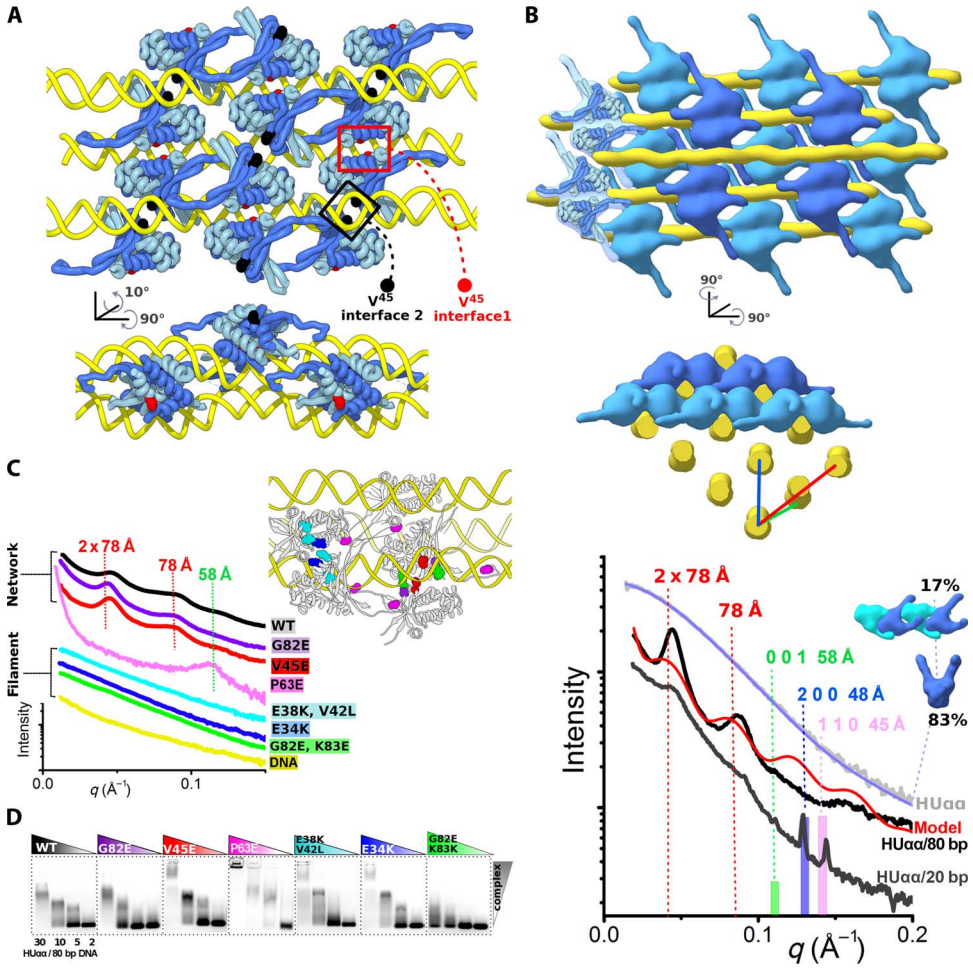

Fig. 2. HUαα-DNA network interactions and assembly. (**A**) Two orthogonal views of HUαα-DNA assembly built by combining multiple crystal asymmetric units along two lateral and one medial DNA. Location of the phosphate lock is highlighted with V^{45} residues. (**B**) Two orthogonal views of the HUαα-DNA nucleoprotein network displayed in molecular surface. The bottom panel shows experimental SAXS of the 16× HUαα/80-bp DNA complex, 8× HUαα/20-bp DNA, and free HUαα with the diffraction peaks at the spacings corresponding to the distances between DNAs as indicated. The red line indicates theoretical SAXS calculated from the two parallel DNAs matching observed SAXS oscillations. SAXS curve of the HUαα–20-bp DNA complex shows sharper peaks due to a more ordered assembly with the peaks matching the reflections (*hkl*: 001, 200, 110) of the crystal structure related to the highlighted distances. SAXS of free HUαα matches the theoretical profile (blue) of an oligomeric mixture as indicated. (**C**) SAXS for 18× HUαα, 13× $HU\alpha\alpha^{G82E}$, 16× $HU\alpha\alpha^{V45E}$, and 5× $HU\alpha\alpha^{P63E}$ with 80-bp DNA shows the diffraction peaks indicating the DNA networks. Note that the $HU\alpha\alpha^{P63E}$ mutant is missing the first diffractions at $d \sim 78$ and $d \sim 2 \times 78$ Å, suggesting disruption of the medial DNA network. SAXS for 10× $HU\alpha38\alpha38^{E38K,L42V}$, 18× $HU\alpha\alpha^{E34K}$, and 19× $HU\alpha\alpha^{G82E,K83E}$ with 80-bp DNA shows the absence of peaks indicating filament-like assemblies. WT, wild type. (**D**) Electrophoretic mobility shift assay (EMSA) gel for each mutation at homodimer/80-bp DNA ratios of 30:1, 10:1, 5:1, and 2:1 at a DNA concentration of 0.0027 mM.

biophysical (*26*, *27*) and imaging experiments (*28*). Our structures show variability in the HU-DNA interfaces (Fig. 1E) that allows DNA binding in the HU saddle at low-salt concentration (*29*, *30*) or binding of short DNAs strands (*31*) where cooperative HUαβ multimerization could not persist. To further test implications of our crystal structures, we collected SAXS data on the 1× HUαβ/20-bp DNA complex. Models derived from crystal structures give an excellent match with the SAXS, whereas the model with the DNA bound to the HUαβ saddle does not (Fig. 3C and fig. S6D). HUαβ can transform the HUαα/80-bp DNA network into filaments, as shown by diminished diffraction peaks upon adding HUαβ into the preformed DNA network (fig. S7A). In considering the combined structural implications for a distinct role of HUαβ in DNA condensation, we posit that HUβ subunits are a foil for HUα action.

A charge blocking assembly switch synchronizes activation of virulence genes

To examine how altered HU multimerization affects the transcription profile, we determined the structure of the DNA-bound $HU\alpha^{E38K,V42L}$ mutant (HUα38). Similar to wild type, HUα38α38 interacts with DNA through interfaces 1 and 2, although only interface 1 supports continuous DNA (Fig. 4A and fig. S1C). Weak electron densities of noncontinuous DNA visible at interface 2 suggest an inability of HUα38α38 to network DNAs (fig. S1C). The surface-exposed K38

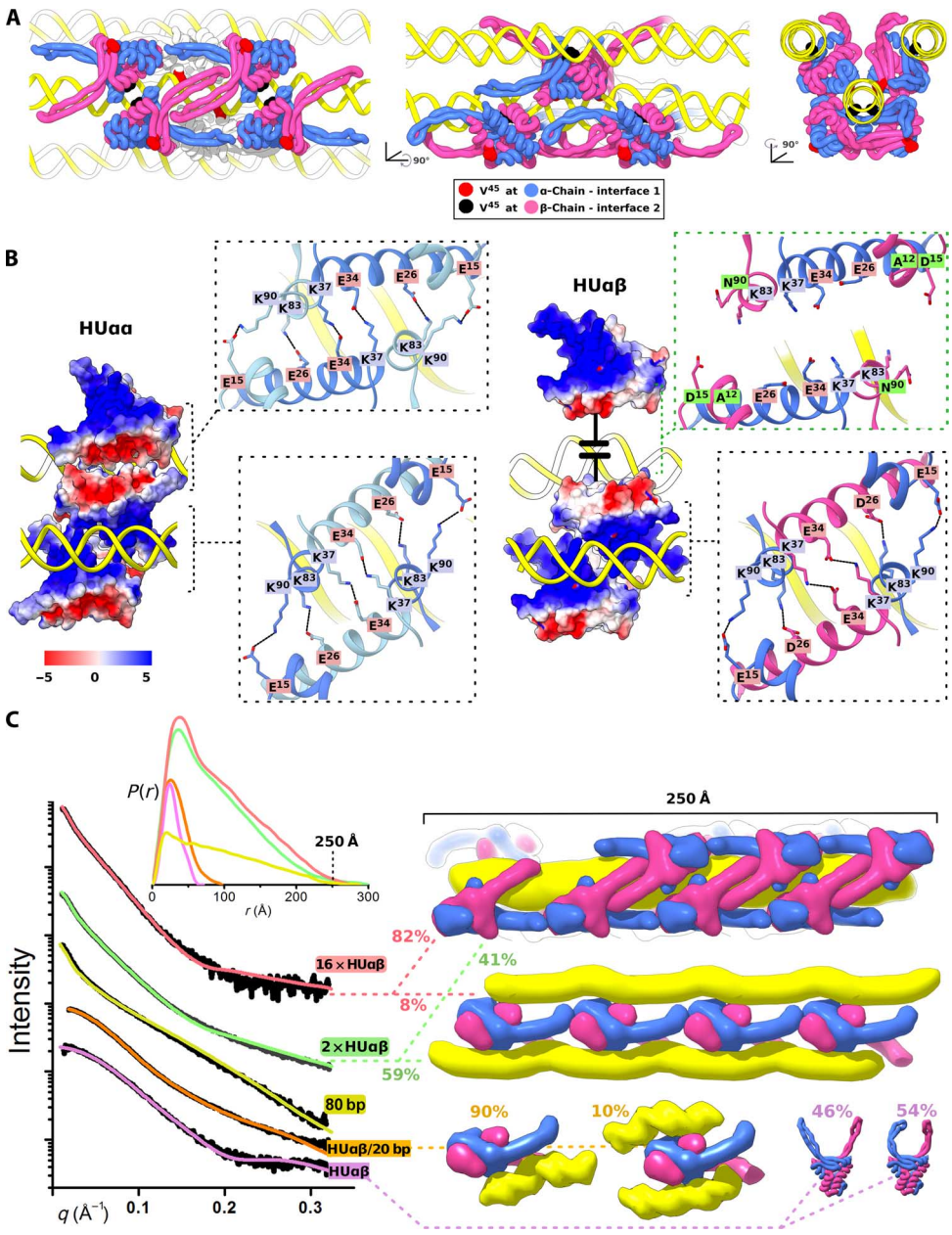

Fig. 3. HUαβ-DNA interactions and assembly. (**A**) Three orthogonal views of HUαβ-DNA assembly along DNA. Assembly from six asymmetric units of the HUαβ–19-bp DNA crystal structure. Location of the phosphate lock is indicated with V^{45} residues. (**B**) Comparison of the electrostatic surfaces of HUαα-HUαα-HUαα and HUαβ-HUαβ coupling across the DNA. HUαβ-HUαβ couples that interact across the DNA do not multimerize with laterally positioned HUαβ. Close-up views highlight the network of hydrogen bonds required for HUαα and HUαβ coupling. The substitution of K90N, E15D, and E12A in the β-chain (green labels) suggests disruption of the hydrogen bond network required for lateral multimerization. (**C**) Experimental SAXS curves for 16× HUαβ/80-bp DNA, 2× HUαβ/80-bp DNA, 80-bp DNA, 1× HUαβ/20-bp DNA, and free HUαβ matching profiles calculated for an ensemble of two atomistic models (low-resolution molecular surfaces). *P*(*r*) functions of the corresponding SAXS curves are normalized by volumes determined by SAXS (*25*) and indicated in Fig. 4D. *P*(*r*) functions indicate maximal dimensions between 250 and 290 Å and volumes of assemblies, which are consistent with atomistic models.

mutation creates a positive charge that alters the original electrostatic surface acting in HUαα-HUαα coupling (Fig. 4B). New coupling through Q^5-D^8 hydrogen bonding is formed (Fig. 4B). Disruption of wild-type coupling allows an arm-to-tail multimerization of HUα38α38 along the DNA (Fig. 4A). Two HU chains in forward and backward directions along the DNA create a grooved U-shaped channel holding DNA (Fig. 4A and movie S4). Eight HUα38α38s form one superhelical turn, allowing alignment of 80-bp DNA located at the base of the grooved DNA binding surface (Fig. 4C).

To visualize HUα38α38-DNA assemblies in solution, we measured SAXS at various protein/80-bp DNA ratios. The filament-like assemblies built along 80-bp DNA not only are consistent with the maximal

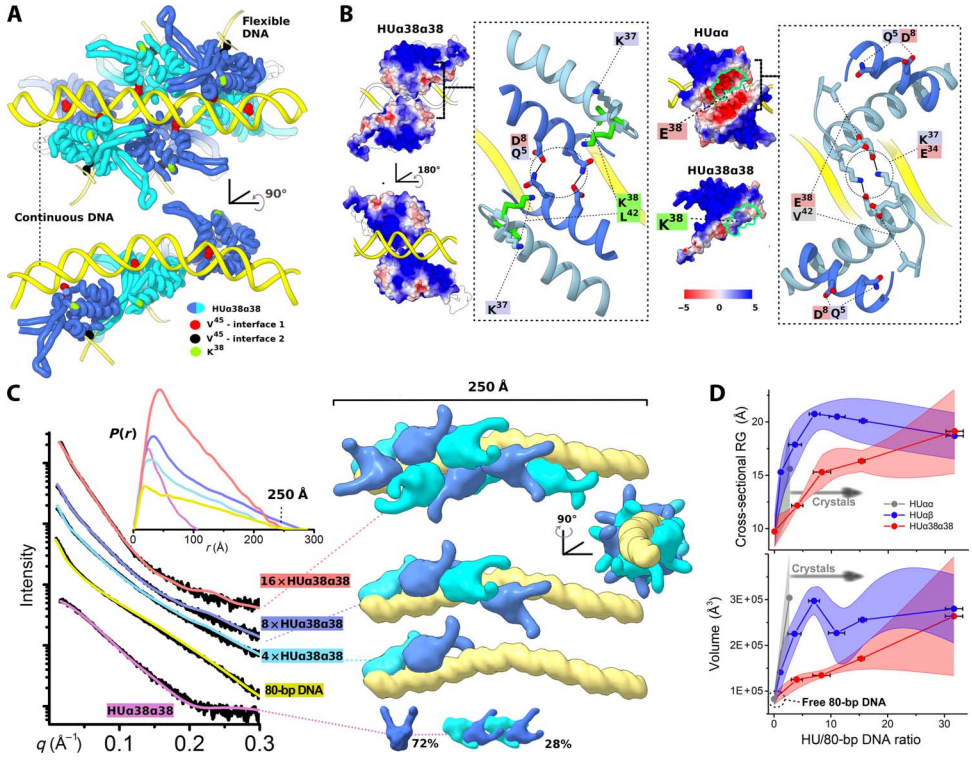

Fig. 4. HUα38α38-DNA interactions and assembly. (**A**) Two orthogonal views of HUα38α38 assembly along DNA. Alternating HUα38α38s are shown for six asymmetric units of the HUα38α38–19-bp DNA crystal structure. V^{45} residues and the K38E mutation are highlighted. (**B**) Arrangements of HUα38α38-HUα38α38 and HUαα-HUαα coupling across DNA are shown as electrostatic surfaces. The right panel shows changes in the electrostatic surface between HUαα and the HUα38α38 mutant. Close-up views highlight the network of hydrogen bonds required for coupling of HUα38α38-HUα38α38. Mutations E38K and V42L are highlighted in green. (**C**) Experimental SAXS curves for 16× HUα38α38/DNA, 8× HUα38α38/DNA, and 4× HUα38α38/DNA ratios and for free HUα38α38 matching the theoretical profiles of atomistic models shown in the right panel (see also fig. S8). Multiple asymmetric units along 80-bp DNA are displayed as low-resolution molecular surfaces. *P*(*r*) functions (inset) were calculated from the corresponding SAXS curves and normalized based on experimentally determined volumes of assemblies (*25*) indicated in (D). *P*(*r*) functions indicate maximal dimensions between 250 and 290 Å and volumes of assemblies, which are consistent with atomistic models. (**D**) SAXS-determined cross-sectional R_G's and volumes show the formation of HUαβ/80-bp DNA complexes that are thicker and bulkier than HUα38α38/80-bp DNA complexes. These parameters cannot be determined for crystalline HUαα complexes formed at the >3× HUαα/80-bp DNA ratio.

dimension of 250 Å or with the volume of particles determined by SAXS but also fit the experimental curves well (Fig. 4C and fig. S8). Smaller cross-sectional radii of gyration and volumes derived from SAXS (Fig. 4D) in relation to HUαβ/80-bp DNA suggest that HUα38α38s do not bridge DNAs but rather spread out on independent DNAs. HUα38α38-DNA SAXS parameters, together with derived models, correlate with observed nucleoprotein particles shown by atomic force microscopy (AFM) (*32*), which are in contrast to bridged HUαβ nucleoprotein particles also seen by AFM (*28*). However, similar to HUαβ, HUα38α38 transforms the HUαα/80-bp DNA network into filaments, as seen by diminishing diffraction peaks after adding HUα38α38 (fig. S7B). The inability of the HUα38 mutation to network or bridge DNAs links such mutation to increased DNA superhelicity in vivo (*32*) (fig. S9).

To test the implications of our in vitro HU-DNA complexes for nucleoid structural changes occurring upon HUβ and ectopic HUα38 expression, we imaged *E. coli* wild-type MG1655 and mutant HUα38 (SK3842) strains with SXT. SXT is a high-resolution imaging method that is applied to fully hydrated, unfixed, and unstained cells and that directly measures carbon and nitrogen concentration in biological samples (*33*). Orthoslices and three-dimensional (3D) reconstructions of SXT imaging of MG1655 in the early growth phase reveal the expected spreading out of dispersed nucleoid with a lobular structure (Fig. 5A). Local nucleoid condensation in wild type was visible during all stages of cell cycle (from a resting cell to a newly divided cell) (Fig. 5A). Changes in nucleoid condensation are linked to HUβ expression, which supports negative supercoiling (*20*) (fig. S9). Thus, cellular HU-DNA assembly is a dynamic equilibrium between HUαα and HUαβ, where HUαβ-DNA patches (*3*, *34*) alternate with an HUαα-HUαα network (fig. S9). This alteration of HU multimerization appears suitable for changing accessibility to factors, such as DNA gyrase or topoisomerase (*1*) to maintain DNA supercoiling and provide a mechanism for HUαβ to dictate the global transcription profile. In contrast, the nucleoid in the mutant SK3842 strain was organized into a densely condensed unit in all growth phases (Fig. 5A, bottom). As we showed previously, nucleoid condensation observed in the mutant is a direct effect of HUα38 and not mediated through other nucleoid-condensing proteins, such as H-NS and Dps or higher levels of the mutant HU (*15*). Overall, nucleoid condensation induced by HUβ and HUα38 expression can be quantified using the nucleoid volume and linear absorption coefficient (LAC) (Fig. 5B). Although the HUβ expression in the late growth phase decreases the nucleoid volume from 3.5 to 1.5 μm^3, induced condensation by ectopic

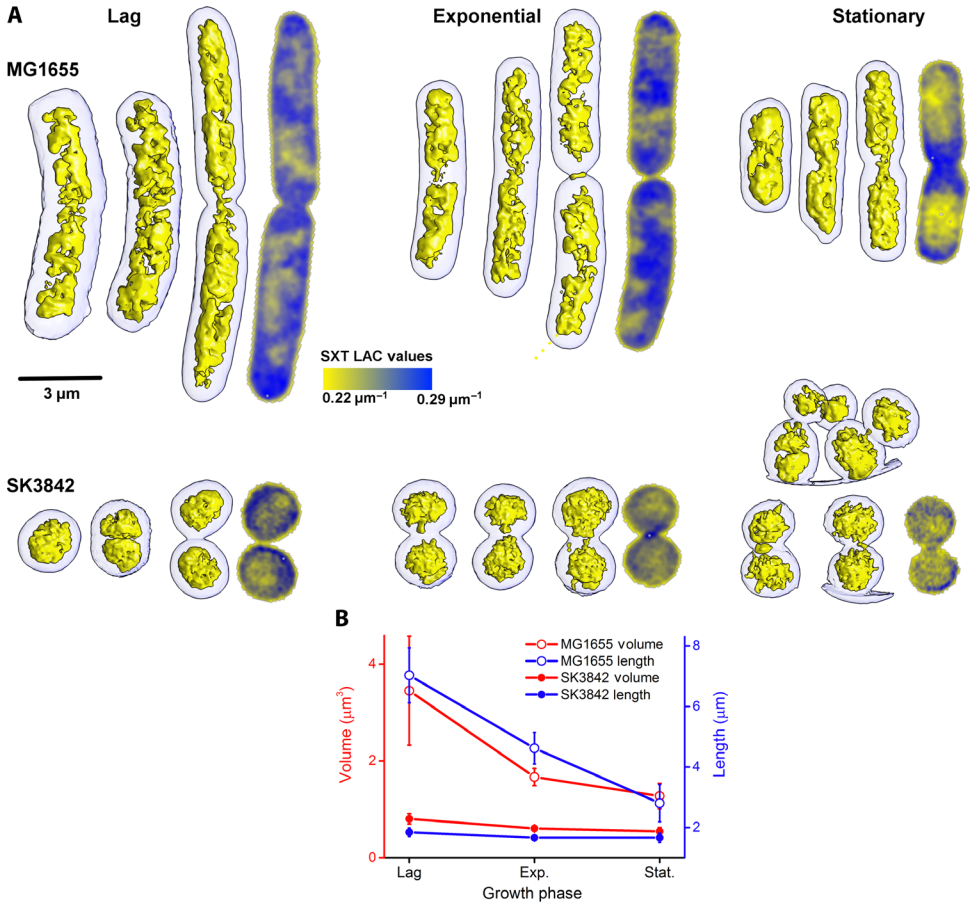

Fig. 5. Nucleoid condensation upon HUβ and ectopic HUα38 expression. (**A**) SXT displays nucleoid organization for WT MG1655 and mutant HUα38 (SK3842) *E. coli* strains at all stages of the cell cycle. Three representative reconstructions are shown for the lag, exponential, and stationary phase. Nucleoid volume (yellow surface rendering) was segmented from the tomographic reconstruction using the 3D LAC at LAC = 0.25 μm^{-1}. A representative orthoslice for the nonsegmented image is shown for each growth phase within the LAC = 0.22 to 0.29 μm^{-1} (yellow to blue). (**B**) Quantification of the total volume of the nucleoid by SXT at LAC = 0.25 μm^{-1} revealed that MG1655 cells in the late growth phase had a decreased nucleoid volume from 3.5 to 1.5 μm^3. Condensation in SK3842 is more marked with a nucleoid volume of <1 μm^3 in all growth phases.

HUα38 expression is strikingly more marked with a nucleoid volume of <1 μm^3 in all growth phases (Fig. 5B).

For HU and nucleoid architecture, the molecular functionality key to macroscopic behavior begins to manifest itself at the nanoscale and extends into the mesoscale (or middle area) that uncovers the emergence of collective behavior. Rather than site-specific DNA bending, HUβ expression condenses the chromosome (Fig. 5) and supports negative supercoiling (*20*). We find that this occurs via disruption of DNA networks by inducing DNA patches that transform periodic DNA condensation into more superhelical structures (fig. S9). Furthermore, altering HU surface charges shows how HU can play regulatory roles in the acidic stress response in *Helicobacter pylori* (*35*) and uncovers a mechanism of gene regulation by altering HU. The *E. coli* HUα38α38 mutant shows a markedly condensed chromosome that is directly linked to positive supercoiling (*32*). The structural characterization of HUα38-DNA presented here thus links HU charges to cooperative multimerizations that in turn help control DNA supercoiling (fig. S9).

Using these combined multiscale structures, we define a mechanism whereby the level and type of superhelicity are automatically generated through an altered mode of supercoil restraints rather than requiring changes in cellular topoisomerase activities (*15*). These data therefore support a unified, testable model for the relationships of HU structural assemblies and networks with compaction and transcription that explains and extends multiple observations. The shift in HU's multimerization provides an efficient general mechanism to synchronize the genetic response to external conditions. Furthermore, effector molecules present in pathogenicity-inducing environments may elicit changes in HU-mediated nucleoid condensation, leading to swift and concerted changes in the basal transcription program. These observations make HU interactions an attractive target for controlling not only pathogenesis but also microbial systems in general.

MATERIALS AND METHODS

Protein purification

HUαβ was purified from an expression plasmid (pRLM118) (*36*). HU-hyperexpressing cells were grown at 30°C in 200 ml of LB medium

containing ampicillin (100 μg/ml) to an A_{600} (absorbance at 600 nm) of 1.5. The culture was quickly placed in a water bath at 42°C and was shaken for 30 min. The cells were washed once and suspended in 50 ml of buffer [20 mM Hepes-NaOH (pH 7.5), 60 mM KCl, and 1 mM dithiothreitol (DTT)] and disrupted by passing through a French press three times. After removing the cell debris by centrifugation at 7000*g* for 10 min, the supernatant was fractionated by ammonium sulfate precipitation at 70 to 90% saturation. The ammonium sulfate precipitation was repeated twice. The fraction rich in HUαβ was loaded on a 10-ml Q-Sepharose column (Pharmacia Biotech) pre-equilibrated with buffer. A flow-through fraction was taken and directly applied on a 5-ml heparin-Sepharose column (Pharmacia Biotech) pre-equilibrated with buffer. After thoroughly washing the column with buffer containing 400 mM KCl, HU was eluted by a linear gradient with buffer containing 1.2 M KCl. Eluate at 0.6 to 0.8 M KCl was taken and stored at −80°C. Protein concentration was measured by using the BCA Protein Assay Kit (Pierce) with bovine serum albumin (BSA) as standard.

HUα, HUα mutants (HUα38^{E38K,V42L}, HUα^{E34K}, HUα^{V45E}, HUα^{G82E}, and HUα^{G82E,K83E}), and hupA genes were cloned in expression vector pET15b (Novagen) and transformed into BL21(DE3)pLysS strains. Cells were grown in 2 × 600 ml of ZYM-5052 autoinduction medium in 2-liter flasks. Cells were grown at 37°C for 5 hours, and then the temperature was decreased to 20°C; cells were allowed to induce for 19 hours thereafter. After induction, cells were harvested by centrifugation and resuspended in buffer A [10 mM Hepes (pH 7.9), 0.5 M NaCl, and 5 mM imidazole], with an additional 0.1% Triton X-100, 2 mM phenylmethylsulfonyl fluoride (PMSF), lysozyme (0.5 mg/ml), DNase I (50 μg/ml), 20 μM $CaCl_2$, and 4 mM $MgCl_2$. Cells were lysed by passage through a constant cell disruptor (Constant Systems Ltd.) at 5°C and 21 kpsi. After lysis, cellular debris was pelleted by centrifugation. Cleared cell lysate was batch-bound onto Ni-NTA (nitrilotriacetic acid) resin (Qiagen) by rocking overnight at 4°C. Resin was batch-washed in buffer A and then washed with 10× column volume (CV) buffer A + 20 mM imidazole. Elution was carried out with 10× CV buffer A + 250 mM imidazole. Ni-NTA eluate was dialyzed into buffer B [2 mM Hepes (pH 7.9) and 20 mM NaCl] in a 3.5K MWCO Slide-A-Lyzer (Thermo Scientific). Dialysate was then purified by cation exchange chromatography on a HiTrap SP HP column (GE Healthcare). Protein was bound onto the column and then eluted with a gradient starting from buffer B to buffer B + 1 M NaCl. HU was concentrated to a final concentration of 3 to 4 mg/ml on 3.5K MWCO Vivaspin ultrafiltration devices (GE Healthcare) and stored at −80°C.

The protein concentration of all purified HUs was determined by Bradford and Lowry assays. The Bradford assay consists of mixing 1.0 ml of Bradford reagent (Bio-Rad) with 20 μl of protein and allowing the mixture to react for 10 min at room temperature. A_{595} was then measured on an Agilent 8453 UV-visible spectrophotometer. BSA (Thermo Scientific) was used as a standard. Concentrations of HU were verified with a modified Lowry assay (Thermo Scientific).

DNA purification

The 80-, 20-, and 19-bp blunt-end dsDNAs are highly purified synthetic DNAs. Nineteen–base pair DNA (5′-TTCAATTGTTGTTAACTTG-3′), 20-bp DNA (5′-GTTCAATTGTTGTTAACTTG-3′), and 80-bp DNA (5′-AATGAGGTAACAACGAAAGCAGATGATAGCTGCTTATCAATTTGTTGCAAACAAGTAGCCGCGCCCAATGAGGTAACAAT-3′) were dissolved and annealed in water. Annealed DNAs were purified by size exclusion chromatography on a Shodex KW402 column using 50 mM bis-tris (pH 6.0) running buffer.

Crystallization

To aid in the efficient crystallization of HU in complex with native duplex DNA, we used SAXS to optimize sequence-independent DNA interactions with HU in solution and to seek effective crystallization conditions by optimizing interactions that are suitably ordered in solution. We tested various lengths of native DNA duplexes with and without 1-bp overhangs. SAXS of HUαα-DNA complexes showed diffraction peaks where the maximal resolution and sharpness of the peak suggest complexes suitable for crystallization. SAXS of HUαβ-DNA and HUα38α38-DNA did not show a diffraction peak. In these cases, SAXS was used to define Porod volume and Porod coefficient, which indicate the intrinsic flexibility of the complex (*37*) and which can be linked to the suitability of complexes for crystallization. The 19- and 20-bp blunt-end DNAs were selected for further crystallization studies. We also obtained crystals containing DNA with 1-bp overhangs and 18-bp blunt-end DNA. DNA for crystallization was concentrated to ~7.0 mg/ml. HUαα, HUαβ, and HUα38α38 were dissolved in 50 mM tris-Cl (pH 7.5), 100 mM NaCl, and 5% glycerol, and concentrated to ~20 mg/ml before crystallization.

Crystals were grown by hanging-drop vapor diffusion. For HUαα–19-bp DNA, 0.5 μl of 19-bp DNA diluted in 0.5 μl of 0.1 M bis-tris (pH 5.5), 20% polyethylene glycol (PEG) 3350, and 0.2 M NH_4F was mixed with 1 μl of HUαα and dehydrated over 800 μl of 0.1 M bis-tris (pH 5.5), 20% PEG3350, and 0.2 M NH_4F. For HUαα–20-bp DNA, 1 μl of 20-bp DNA diluted in 0.5 μl of 0.1 M bis-tris (pH 6.5), 45% 2-methyl-2,4-pentadiol, and 0.2 M NH_4F was mixed with 1 μl of HUαα and dehydrated over 800 μl of 0.1 M bis-tris (pH 6.5), 45% 2-methyl-2,4-pentadiol, and 0.2 M NH_4F. For HUαβ–19-bp DNA and HUαβ–20-bp DNA, 1 μl of 19- or 20-bp DNA diluted in 0.7 μl of 0.1 M bis-tris (pH 6.5), 30% PEG monomethyl ether (MME) 550, and 0.05 M $CaCl_2{\cdot}2\times H_2O$ was mixed with 0.7 μl of HUαα and dehydrated over 800 μl of 0.1 M bis-tris (pH 6.5), 30% PEG MME 550, and 0.05 M $CaCl_2{\cdot}2\times H_2O$. For HUα38α38–19-bp DNA and HUα38α38–20-bp DNA, 1.5 μl of DNA diluted in 1 μl of 0.1 M bis-tris (pH 5.8), 30% PEG MME 550, 0.05 M $CaCl_2{\cdot}2\times H_2O$, and 10% glycerol was mixed with 1 μl of HUαα and dehydrated over 800 μl of 0.1 M bis-tris (pH 5.8), 30% PEG MME 550, 0.05 M $CaCl_2{\cdot}2\times H_2O$, and 10% glycerol. The best diffraction crystals grew in the drops produced by streaking protein into the DNA drop. Crystals grew in 2 to 3 days at 20°C.

Data collection and structural analysis

Structures of HU-DNA complexes were solved by molecular replacement with x-ray diffraction data collected from cryocooled crystals at the SIBYLS Beamline BL 12.3.1 (*38*) and BL 8.3.1 of the Advanced Light Source (ALS). The data were reduced with autoPROC (*39*), and the phases were defined by molecular replacement in PHASER (*40*) using the refined structure of HUαα or HUαβ [Protein Data Bank (PDB) ID: 1MUL (*19*) or 2O97 (*20*), respectively]. The molecular replacement phases yielded clear density for dsDNA. Ideal DNA helices were placed manually into the density, and the model was subjected to maximum-likelihood refinement using BUSTER with LSSR restraints (*41*) from the molecular replacement model. The side chains were built using sigmaA- weighted $2F_o - F_c$ and $F_o - F_c$ maps in COOT (*42*) (table S1). Structures were visualized in Chimera (*43*). Electrostatic surface potential were calculated using Adaptive Poisson-Boltzmann Solver at pH 7.0 (*44*). To correlate

SAXS diffraction peaks with our HUαα-DNA structure (Fig. 2B), we calculated structure factors from the crystal structure with PHENIX.FMODEL (*45*) and transferred them into the reflection data file with MTZDUMP (*46*). Atomic coordinates and structure factors for the crystal structures were deposited in the PDB under accession codes 4YEX, 4YEY, 4YFH, 4YF0, 4YFT, and 4YEW.

SAXS data collection and evaluation

SAXS data were collected at the ALS beamline 12.3.1 (SIBYLS), Lawrence Berkeley National Laboratory (Berkeley, CA) (*47*) for HU concentrations of 17 to 200 μM spanning the measured intracellular HU concentrations of 25 to 100 μM (*48*). The wavelength was set to λ = 1.0 Å and the sample-to-detector distance was set to 1.5 m, resulting in scattering vectors, with q ranging from 0.01 to 0.32 $Å^{-1}$. The scattering vector is defined as $q = 4\pi \sin\theta/\lambda$, where 2θ is the scattering angle. All experiments were performed at 20°C, and data were processed as previously described (*47*). The buffer for SAXS experiments was 50 mM tris-HCl (pH 7.5), 150 mM NaCl, 1 mM DTT, and 1 mM PMSF. To collect SAXS for protein-DNA assemblies, proteins HUαα, HUαβ, and HUα38α38, respectively, were mixed with DNA directly before the data collection (~5 min) at the protein/DNA ratios, as indicated in figs. S5, S6, and S8. The SAXS curve of HUαα-DNA showed diffraction peaks, indicating the formation of a crystalline phase in solution. These SAXS experiments revealed diffraction peaks defining the d spacing between parallel DNAs. This type of SAXS curve cannot be used to obtain the pair distribution function [$P(r)$] or radius of gyration (R_G). Observed diffraction peaks in HUαα–20-bp DNA samples were identical with the lattice planes calculated for the refined HUαα-DNA crystal structure. The theoretical scattering profiles for two parallel DNAs, as indicated in Fig. 2B, were calculated with FoXS (*49*). To test disruption of the HUαα–80-bp DNA network, we titrated HUαβ (fig. S7A) or HUα38α38 (fig. S7B) into the preformed HUαα–80-bp DNA assembly (HUαα/DNA ratio, 17:1; DNA concentration, 0.02 mM). The relative level of networking was quantified by calculating the area under the diffraction peak within the q range of 0.07 to 0.11 $Å^{-1}$ and normalizing it to the area of the peak for the initial HUαα/80-bp DNA assembly (fig. S7). SAXS curves of free proteins, free DNAs, or HUαβ-DNA and HUα38α38-DNA assemblies did not show diffraction peaks and were merged and further analyzed as previously reported (*50*). Aggregation-free states of samples were investigated by defining the linear region in the Guinier plots (*51*) (figs. S6B and S8B). Cross-sectional radius of gyration and Porod volume (*52*) were calculated by the program ScÅtter for three independent HUαα/80-bp DNA, HUαβ/80-bp DNA, and HUα38α38/80-bp DNA titration experiments (Fig. 4D). $P(r)$ functions were calculated by the program GNOM (*53*). The distance r where $P(r)$ functions approach zero intensity identifies the maximal dimension (D_{max}) of the macromolecule (Figs. 3C and 4C, and figs. S6C and S8C). $P(r)$ functions were normalized based on Porod volumes of assemblies, as calculated by ScÅtter and listed in table S2 (Figs. 3C and 4C), or based on their maxima (figs. S6C and S8C).

SAXS modeling

To match SAXS curves of different HUαβ/80-bp DNA and HUα38α38/80-bp DNA ratios to various HU-DNA binding modes, we applied ensemble analysis (*54*, *55*). This approach introduces the concept of ensemble fitting of the SAXS data from multicomponent systems. A large pool (more than 20) of various HU/DNA complexes (covering one, two, or three neighboring 80-bp DNAs) was generated based on the crystal structures. A sub-ensemble of complexes coexisting in solution was selected by a genetic algorithm guided by the fit to the experimental SAXS data using FoXS-MES (Minimal Ensemble Search) (*49*, *56*). The selected complexes were weighted, allowing the selection of the minimal ensemble to avoid overfitting with the larger ensemble. The size of the minimal ensemble was selected based on the level of improvement in the SAXS fit between different ensemble sizes. HUαβ/80-bp DNA data were matched with an ensemble of two different complexes. The match of theoretical profiles to the experimental curve could be improved with larger ensemble sizes; however, an ensemble size of two for HUαβ/80-bp DNA (Fig. 3C and fig. S6) and one for HUα38α38/80-bp DNA (Fig. 4C and fig. S8) was sufficient to fit the data. Ensemble modeling was also applied to determine the solution state of 1× HUαβ/20-bp DNA (Fig. 3C and fig. S6). The various atomistic models of HUαβ/20-bp DNA were built by combining multiple positions of one or two 20-bp DNA along with one HUαβ as seen in their crystal structure. An alternative model with the 20-bp DNA located between HUαβ extended arms was built by positioning DNA according to previously reported HU crystal structures with specific DNA (*21*). A FoXS-MES approach was applied to define a minimal ensemble of two, as shown in Fig. 3C and fig. S6D. The oligomeric mixture of free HUαα and free HUα38α38 was determined by a FoXS-MES approach. Higher oligomeric states of HUαα were built based on the crystal packing reported for the *Bacillus anthracis* HU structure (PDB ID: 3RHI). A BILBOMD approach (*56*) was used to explore the flexibility of HUαβ extended arms in free state (Fig. 3C). BILBOMD uses molecular dynamics (MD) simulations to explore the conformational space of the extended arms. The MD simulations provide an ensemble of molecular models from which a SAXS curve is calculated and compared to the experimental curve. A genetic algorithm (MES) (*56*) was used to select and weight two conformers, which best fit the SAXS curve of HUαβ. SAXS data and SAXS-derived models were deposited with the BIOISIS database, and experimental SAXS parameters are reported in table S2.

Soft x-ray microscopy

E. coli strain MG1655 and HUα38 mutant strain SK3842 were used for SXT. Mutagenesis of HUα38 and integration of the mutant *hupA* gene into the chromosome have been previously described by Kar and Adhya (*57*). Cells were grown in 5 ml of LB medium at 37°C. Cells were put on ice and promptly cryoimmobilized after reaching an OD_{600} (optical density at 600 nm) of 0.2 for the lag phase, 0.5 for the exponential phase, and >1.0 for the stationary phase. Cells were mounted in thin-walled glass capillary tubes and rapidly cryoimmobilized before being mounted in the cryogenic specimen rotation stage of the XM-2 soft x-ray microscope at the National Center for X-ray Tomography (ALS). Each data set (that is, 90 projection images spanning a range of 180°) was collected using a microscope equipped with a Fresnel zone plate–based objective lens with a resolution of 50 nm (*58*). The projections for every tilt were recorded using a Peltier-cooled, back-thinned, and direct-illuminated 2048 × 2048 pixel soft x-ray charge-coupled device camera (Roper Scientific iKon-L). Projection images were manually aligned using IMOD software by tracking fiducial markers on adjacent images. The 3D x-ray tomograms were segmented using Chimera (*43*) and were used to reconstruct volumes, measure voxel values (that is, absorption values in the volume element of the reconstructed data), and calculate LACs. To quantitatively compare the volume and length of a nucleoid for various cells, x-ray tomograms were filtered with a Gaussian filter and segmented at LAC = 0.25 $μm^{-1}$. Ten cells per growth phase were used to calculate the volume and length of a nucleoid

(Fig. 5B) with the exception of the MG1655 lag phase where five cells were reconstructed. Orthoslices and volumetric reconstructions of nucleoid were displayed in Chimera (Fig. 5A) (*43*).

Electrophoretic mobility shift assay

EMSAs were performed for HUα and HUα mutants (HUα38^{E38K,V42L}, HUα^{E34K}, HUα^{V45E}, HUα^{G82E}, and HUα^{G82E,K83E}). EMSAs were run on 1.1% agarose gels in 1× tris-acetate-EDTA buffer and visualized with ethidium bromide. Eighty–base pair DNA (1.5 μg) (1.5 μl at 1 mg/ml) was combined with HU to yield protein/DNA ratios of 30:1, 10:1, 5:1, and 2:1; diluted with buffer [50 mM tris (pH 7.5) and 150 mM NaCl] to 10 μl; combined with loading dye; and run on a gel (at 200 V for 20 min).

SUPPLEMENTARY MATERIALS

Supplementary material for this article is available at http://advances.sciencemag.org/cgi/content/full/2/7/e1600650/DC1

fig. S1. Electron density maps of extended DNA strands and HU arm regions.
fig. S2. Superimposition of two HU-DNA complex faces reveals distinct protein-DNA interfaces.
fig. S3. Structurally informed sequence alignment of HU/IHF family members reveals conservation with functional implications.
fig. S4. Schematic of all protein-protein and protein-DNA interactions.
fig. S5. Experimental SAXS of HUαα-DNA assemblies reveals DNA networks.
fig. S6. SAXS analysis of HUαβ/80-bp DNA indicates formation of filament-like assemblies.
fig. S7. HUαβ and HUα38α38 transform the HUαα/80-bp DNA network into filaments.
fig. S8. SAXS analysis of HUα38α38/80-bp DNA indicates formation of filament-like assemblies.
fig. S9. DNA supercoiling regulated by altering ratios of HUαα/HUαβ.
table S1. X-ray diffraction data collection and refinement statistics (molecular replacement).
table S2. SAXS data collection and analysis parameters.
movie S1. Distinct DNA binding modes of HUαα with nonspecific and damaged DNA.
movie S2. Formation of HUαα-DNA assembly.
movie S3. Formation of HUαβ-DNA assembly.
movie S4. Formation of HUα38α38-DNA assembly.

REFERENCES AND NOTES

1. X. Wang, P. Montero Llopis, D. Z. Rudner, Organization and segregation of bacterial chromosomes. *Nat. Rev. Genet.* **14**, 191–203 (2013).
2. C. J. Dorman, Genome architecture and global gene regulation in bacteria: Making progress towards a unified model? *Nat. Rev. Microbiol.* **11**, 349–355 (2013).
3. W. Wang, G.-W. Li, C. Chen, X. S. Xie, X. Zhuang, Chromosome organization by a nucleoid-associated protein in live bacteria. *Science* **333**, 1445–1449 (2011).
4. S. C. Dillon, C. J. Dorman, Bacterial nucleoid-associated proteins, nucleoid structure and gene expression. *Nat. Rev. Microbiol.* **8**, 185–195 (2010).
5. T. A. Azam, A. Ishihama, Twelve species of the nucleoid-associated protein from *Escherichia coli*. Sequence recognition specificity and DNA binding affinity. *J. Biol. Chem.* **274**, 33105–33113 (1999).
6. L. Claret, J. Rouviere-Yaniv, Variation in HU composition during growth of *Escherichia coli*: The heterodimer is required for long term survival. *J. Mol. Biol.* **273**, 93–104 (1997).
7. D. Kamashev, J. Rouviere-Yaniv, The histone-like protein HU binds specifically to DNA recombination and repair intermediates. *EMBO J.* **19**, 6527–6535 (2000).
8. C. I. Vitoc, I. Mukerji, HU binding to a DNA four-way junction probed by Förster resonance energy transfer. *Biochemistry* **50**, 1432–1441 (2011).
9. R. C. Johnson, L. M. Johnson, J. W. Schmidt, J. F. Gardner, Major nucleoid proteins in the structure and function of the *Escherichia coli* chromosome, in *The Bacterial Chromosome*, N. P. Higgins, Ed. (ACM Press, Washington, DC, 2005), pp. 65–131.
10. H. M. Lim, D. E. A. Lewis, H. J. Lee, M. Liu, S. Adhya, Effect of varying the supercoiling of DNA on transcription and its regulation. *Biochemistry* **42**, 10718–10725 (2003).
11. C. J. Dorman, DNA supercoiling and environmental regulation of gene expression in pathogenic bacteria. *Infect. Immun.* **59**, 745–749 (1991).
12. J. D. Helmann, M. J. Chamberlin, Structure and function of bacterial sigma factors. *Annu. Rev. Biochem.* **57**, 839–872 (1988).
13. A. Ishihama, Promoter selectivity of prokaryotic RNA polymerases. *Trends Genet.* **4**, 282–286 (1988).
14. J. Rouvière-Yaniv, M. Yaniv, J.-E. Germond, E. coli DNA binding protein HU forms nucleosome-like structure with circular double-stranded DNA. *Cell* **17**, 265–274 (1979).
15. S. Kar, R. Edgar, S. Adhya, Nucleoid remodeling by an altered HU protein: Reorganization of the transcription program. *Proc. Natl. Acad. Sci. U.S.A.* **102**, 16397–16402 (2005).
16. P. Koli, S. Sudan, D. Fitzgerald, S. Adhya, S. Kar, Conversion of commensal *Escherichia coli* K-12 to an invasive form via expression of a mutant histone-like protein. *mBio* **2**, e00182-11 (2011).
17. C. D. Putnam, M. Hammel, G. L. Hura, J. A. Tainer, X-ray solution scattering (SAXS) combined with crystallography and computation: Defining accurate macromolecular structures, conformations and assemblies in solution. *Q. Rev. Biophys.* **40**, 191–285 (2007).
18. C. E. Blanchet, D. I. Svergun, Small-angle X-ray scattering on biological macromolecules and nanocomposites in solution. *Annu. Rev. Phys. Chem.* **64**, 37–54 (2013).
19. J. Ramstein, N. Hervouet, F. Coste, C. Zelwer, J. Oberto, B. Castaing, Evidence of a thermal unfolding dimeric intermediate for the *Escherichia coli* histone-like HU proteins: Thermodynamics and structure. *J. Mol. Biol.* **331**, 101–121 (2003).
20. F. Guo, S. Adhya, Spiral structure of *Escherichia coli* HUαβ provides foundation for DNA supercoiling. *Proc. Natl. Acad. Sci. U.S.A.* **104**, 4309–4314 (2007).
21. K. K. Swinger, K. M. Lemberg, Y. Zhang, P. A. Rice, Flexible DNA bending in HU–DNA cocrystal structures. *EMBO J.* **22**, 3749–3760 (2003).
22. K. K. Swinger, P. A. Rice, IHF and HU: Flexible architects of bent DNA. *Curr. Opin. Struct. Biol.* **14**, 28–35 (2004).
23. K. W. Mouw, P. A. Rice, Shaping the *Borrelia burgdorferi* genome: Crystal structure and binding properties of the DNA-bending protein Hbb. *Mol. Microbiol.* **63**, 1319–1330 (2007).
24. P. A. Rice, S.-w. Yang, K. Mizuuchi, H. A. Nash, Crystal structure of an IHF-DNA complex: A protein-induced DNA U-turn. *Cell* **87**, 1295–1306 (1996).
25. R. P. Rambo, J. A. Tainer, Accurate assessment of mass, models and resolution by small-angle scattering. *Nature* **496**, 477–481 (2013).
26. J. Koh, R. M. Saecker, M. T. Record Jr., DNA binding mode transitions of *Escherichia coli* $HU_{\alpha\beta}$: Evidence for formation of a bent DNA–protein complex on intact, linear duplex DNA. *J. Mol. Biol.* **383**, 324–346 (2008).
27. L. Czapla, J. P. Peters, E. M. Rueter, W. K. Olson, L. J. Maher III, Understanding apparent DNA flexibility enhancement by HU and HMGB architectural proteins. *J. Mol. Biol.* **409**, 278–289 (2011).
28. J. van Noort, S. Verbrugge, N. Goosen, C. Dekker, R. T. Dame, Dual architectural roles of HU: Formation of flexible hinges and rigid filaments. *Proc. Natl. Acad. Sci. U.S.A.* **101**, 6969–6974 (2004).
29. J. Koh, I. Shkel, R. M. Saecker, M. T. Record Jr., Nonspecific DNA binding and bending by $HU_{\alpha\beta}$: Interfaces of the three binding modes characterized by salt-dependent thermodynamics. *J. Mol. Biol.* **410**, 241–267 (2011).
30. B. Xiao, R. C. Johnson, J. F. Marko, Modulation of HU–DNA interactions by salt concentration and applied force. *Nucleic Acids Res.* **38**, 6176–6185 (2010).
31. R. Boelens, H. Vis, C. E. Vorgias, K. S. Wilson, R. Kaptein, Structure and dynamics of the DNA binding protein HU from Bacillus stearothermophilus by NMR spectroscopy. *Biopolymers* **40**, 553–559 (1996).
32. S. Kar, E. J. Choi, F. Guo, E. K. Dimitriadis, S. L. Kotova, S. Adhya, Right-handed DNA supercoiling by an octameric form of histone-like protein HU: Modulation of cellular transcription. *J. Biol. Chem.* **281**, 40144–40153 (2006).
33. G. McDermott, M. A. Le Gros, C. G. Knoechel, M. Uchida, C. A. Larabell, Soft X-ray tomography and cryogenic light microscopy: The cool combination in cellular imaging. *Trends Cell Biol.* **19**, 587–595 (2009).
34. A. I. Prieto, C. Kahramanoglou, R. M. Ali, G. M. Fraser, A. S. N. Seshasayee, N. M. Luscombe, Genomic analysis of DNA binding and gene regulation by homologous nucleoid-associated proteins IHF and HU in *Escherichia coli* K12. *Nucleic Acids Res.* **40**, 3524–3537 (2012).
35. O. Almarza, D. Nunez, H. Toledo, The DNA-binding protein HU has a regulatory role in the acid stress response mechanism in *Helicobacter pylori*. *Helicobacter* **20**, 29–40 (2015).
36. T. Aki, S. Adhya, Repressor induced site-specific binding of HU for transcriptional regulation. *EMBO J.* **16**, 3666–3674 (1997).
37. R. P. Rambo, J. A. Tainer, Characterizing flexible and intrinsically unstructured biological macromolecules by SAS using the Porod-Debye law. *Biopolymers* **95**, 559–571 (2011).
38. S. Classen, G. L. Hura, J. M. Holton, R. P. Rambo, I. Rodic, P. J. McGuire, K. Dyer, M. Hammel, G. Meigs, K. A. Frankel, J. A. Tainer, Implementation and performance of SIBYLS: A dual endstation small-angle X-ray scattering and macromolecular crystallography beamline at the Advanced Light Source. *J. Appl. Crystallogr.* **46**, 1–13 (2013).
39. C. Vonrhein, C. Flensburg, P. Keller, A. Sharff, O. Smart, W. Paciorek, T. Womack, G. Bricogne, Data processing and analysis with the autoPROC toolbox. *Acta Crystallogr. Sect. D Biol. Crystallogr.* **67**, 293–302 (2011).
40. A. J. McCoy, R. W. Grosse-Kunstleve, P. D. Adams, M. D. Winn, L. C. Storoni, R. J. Read, *Phaser* crystallographic software. *J. Appl. Crystallogr.* **40**, 658–674 (2007).
41. O. S. Smart, T. O. Womack, C. Flensburg, P. Keller, W. Paciorek, A. Sharff, C. Vonrhein, G. Bricogne, Exploiting structure similarity in refinement: Automated NCS and target-structure restraints in *BUSTER*. *Acta Crystallogr. Sect. D Biol. Crystallogr.* **68**, 368–380 (2012).
42. P. Emsley, K. Cowtan, Coot: Model-building tools for molecular graphics. *Acta Crystallogr. Sect. D Biol. Crystallogr.* **60**, 2126–2132 (2004).

43. E. F. Pettersen, T. D. Goddard, C. C. Huang, G. S. Couch, D. M. Greenblatt, E. C. Meng, T. E. Ferrin, UCSF Chimera—A visualization system for exploratory research and analysis. *J. Comput. Chem.* **25**, 1605–1612 (2004).
44. N. A. Baker, D. Sept, S. Joseph, M. J. Holst, J. A. McCammon, Electrostatics of nanosystems: Application to microtubules and the ribosome. *Proc. Natl. Acad. Sci. U.S.A.* **98**, 10037–10041 (2001).
45. P. D. Adams, P. V. Afonine, G. Bunkóczi, V. B. Chen, I. W. Davis, N. Echols, J. J. Headd, L.-W. Hung, G. J. Kapral, R. W. Grosse-Kunstleve, A. J. McCoy, N. W. Moriarty, R. Oeffner, R. J. Read, D. C. Richardson, J. S. Richardson, T. C. Terwilliger, P. H. Zwart, *PHENIX*: A comprehensive Python-based system for macromolecular structure solution. *Acta Crystallogr. Sect. D Biol. Crystallogr.* **66**, 213–221 (2010).
46. M. D. Winn, C. C. Ballard, K. D. Cowtan, E. J. Dodson, P. Emsley, P. R. Evans, R. M. Keegan, E. B. Krissinel, A. G. W. Leslie, A. McCoy, S. J. McNicholas, G. N. Murshudov, N. S. Pannu, E. A. Potterton, H. R. Powell, R. J. Read, A. Vagin, K. S. Wilson, Overview of the *CCP4* suite and current developments. *Acta Crystallogr. Sect. D Biol. Crystallogr.* **67**, 235–242 (2011).
47. G. L. Hura, A. L. Menon, M. Hammel, R. P. Rambo, F. L. Poole II, S. E. Tsutakawa, F. E. Jenney Jr., S. Classen, K. A. Frankel, R. C. Hopkins, S.-j. Yang, J. W. Scott, B. D. Dillard, M. W. Adams, J. A. Tainer, Robust, high-throughput solution structural analyses by small angle X-ray scattering (SAXS). *Nat. Methods* **6**, 606–612 (2009).
48. T. Ali Azam, A. Iwata, A. Nishimura, S. Ueda, A. Ishihama, Growth phase-dependent variation in protein composition of the *Escherichia coli* nucleoid. *J. Bacteriol.* **181**, 6361–6370 (1999).
49. D. Schneidman-Duhovny, M. Hammel, J. A. Tainer, A. Sali, Accurate SAXS profile computation and its assessment by contrast variation experiments. *Biophys. J.* **105**, 962–974 (2013).
50. K. N. Dyer, M. Hammel, R. P. Rambo, S. E. Tsutakawa, I. Rodic, S. Classen, J. A. Tainer, G. L. Hura, High-throughput SAXS for the characterization of biomolecules in solution: A practical approach. *Methods Mol. Biol.* **1091**, 245–258 (2014).
51. A. Guinier, G. Fournet, *Small-Angle Scattering of X-rays* (John Wiley & Sons, New Jersey, 1955).
52. G. Porod, Die Röntgenkleinwinkelstreuung von dichtgepackten kolloiden Systemen. *Kolloid Z.* **124**, 83–114 (1951).
53. D. Svergun, Determination of the regularization parameter in indirect-transform methods using perceptual criteria. *J. Appl. Crystallogr.* **25**, 495–503 (1992).
54. M. Hammel, Validation of macromolecular flexibility in solution by small-angle X-ray scattering (SAXS). *Eur. Biophys. J.* **41**, 789–799 (2012).
55. P. Bernadó, M. Blackledge, Structural biology: Proteins in dynamic equilibrium. *Nature* **468**, 1046–1048 (2010).
56. M. Pelikan, G. L. Hura, M. Hammel, Structure and flexibility within proteins as identified through small angle X-ray scattering. *Gen. Physiol. Biophys.* **28**, 174–189 (2009).
57. S. Kar, S. Adhya, Recruitment of HU by piggyback: A special role of GalR in repressosome assembly. *Genes Dev.* **15**, 2273–2281 (2001).
58. M. A. Le Gros, G. McDermott, C. A. Larabell, X-ray tomography of whole cells. *Curr. Opin. Struct. Biol.* **15**, 593–600 (2005).

Acknowledgments: We thank the SIBYLS beamline (BL 12.3.1) staff, G. Williams for comments, J. Holton and M. Kuzdovich for aiding data collection, F. Guo for early-stage HU purification, and S. Kar for providing *E. coli* strain SK3842. **Funding:** This work was supported by the NIH Structural Cell Biology of DNA Repair Machines (grant P01 CA92584) and NIH grant MINOS (Macromolecular Insights on Nucleic Acids Optimized by Scattering) GM105404 (to M.H. and J.A.T.). SIBYLS beamline efforts to combine SAXS and crystallography at the ALS were supported in part by the U.S. Department of Energy (DOE) program Integrated Diffraction Analysis Technologies. The National Center for X-ray Tomography was supported by the National Institute of General Medical Sciences of the NIH (grant P41GM103445) and the DOE's Office of Biological and Environmental Research (grant DE-AC02-05CH11231). This work was also supported in part by the NIH Intramural Research Program and the Center for Cancer Research of the National Cancer Institute. **Author contributions:** M.H. developed the project with S.A. and performed the structure data collection and analyses with input from J.A.T. D.A., J.-H.C., F.E.R., R.P., and H.Y.H.T. performed some of the experiments. M.H., S.A., C.A.L., and J.A.T. wrote the article with input from all authors. **Competing interests:** The authors declare that they have no competing interests. **Data and materials availability:** Crystal structures were deposited in the PDB under accession codes 4YEX, 4YEY, 4YFH, 4YF0, 4YFT, and 4YEW. SAXS data and solution models were deposited in BIOISIS with the BIOISIS IDs HUaa1P, HUab1P, HUab2Y, HUab3Y, HUa38P, and HUa38Y. All data needed to evaluate the conclusions in the paper are present in the paper and/or the Supplementary Materials. Additional data related to this paper may be requested from the authors.

Submitted 28 March 2016
Accepted 14 June 2016
Published 29 July 2016
10.1126/sciadv.1600650

Citation: M. Hammel, D. Amlanjyoti, F. E. Reyes, J.-H. Chen, R. Parpana, H. Y. H. Tang, C. A. Larabell, J. A. Tainer, S. Adhya, HU multimerization shift controls nucleoid compaction. *Sci. Adv.* **2**, e1600650 (2016).